Selected papers presented at the 15th Symposium of Magnetic Measurements and Modelling SMMM'2025

Hall Sensors Calibration for Operation Above 2 T at 77 K

P. Lasek*, K. Habelok, M. Stępień and K. Gruszczyk

Silesian University of Technology, Faculty of Electrical Engineering, Department of Power Electronics, Electrical Drives and Robotics, Krzywoustego 2, 44-100 Gliwice, Poland

Doi: 10.12693/APhysPolA.149.S132 *e-mail: pawel.lasek@polsl.pl

This paper presents a calibration of seven low-cost CYSJ362A GaAs Hall sensors operating in liquid nitrogen at 77 K and magnetic flux densities above 2 T. A non-magnetic solenoid coil was used as a reference field source, and the sensor response was modeled using polynomial regression of the Hall voltage–flux density characteristic. Statistical model selection identified a fifth-order polynomial as an optimal compromise between accuracy and model complexity. Measurement uncertainty was quantified using analytical error propagation combined with Monte Carlo simulation, accounting for current measurement, coil geometry, and sensor positioning. The dominant contribution to the uncertainty was the current measurement (approximately 3%), while for magnetic flux densities above 2 T, the combined standard uncertainty reached approximately 10%. The results demonstrate good repeatability under pulsed excitation and confirm the suitability of low-cost GaAs Hall sensors for multi-point magnetic field measurements in high-temperature superconductor experiments.

topics: Hall effect sensors, calibration, high-temperature superconductors (HTS), pulsed-field magnetization

1. Introduction

Hall-effect sensors are widely employed for magnetic field measurements due to their compact size, robustness, and direct voltage output. For cryogenic and high-field applications, commercially available GaAs- and InAs-based Hall probes provide well-characterized performance over wide temperature ranges, often extending down to 1.5 K, and magnetic flux densities of several tesla. Such sensors are routinely used in precision magnetometry and superconducting magnet diagnostics [1].

Accurate magnetic field measurements under cryogenic conditions are essential in many areas of applied physics, including the characterization of high-temperature superconductors (HTS). In particular, pulsed-field magnetization (PFM) is a promising technique for generating large trapped magnetic fields in bulk superconductors and coated conductors [2]. Reliable flux density data are required for modeling flux penetration, analyzing losses, and validating numerical simulations [3].

However, the requirements of PFM experiments differ from those of single-point precision measurements. During PFM, the magnetic field distribution within and around the superconductor is strongly non-uniform and time-dependent, making spatially resolved field measurements necessary [4, 5]. Consequently, multiple Hall sensors are typically deployed simultaneously, often more than seven. In this context, the use of instrumentation-grade commercial cryogenic Hall probes becomes economically impractical and experimentally restrictive, particularly when sensors are exposed to large field gradients, rapid field variations, and mechanical or thermal stresses.

As a result, many experimental HTS systems rely on arrays of low-cost Hall sensors that are not originally intended for operation at cryogenic temperatures or in multi-tesla magnetic fields. In such cases, the lack of dedicated calibration procedures can lead to significant systematic errors, limited reproducibility, and poor comparability between experiments. Developing a reliable and well-documented calibration methodology for these sensors is therefore essential for ensuring the quantitative validity of pulsed-field magnetization measurements.

Reliable operation of Hall sensors at cryogenic temperatures and in magnetic fields exceeding 2 T presents significant technical challenges. Reported issues include nonlinear response, temperature-dependent sensitivity, offset drift, and increased susceptibility to electrical noise [6]. Importantly, many commercially available low-cost Hall sensors are not specifically designed or specified for operation under cryogenic conditions, high magnetic flux densities, or elevated supply voltages.

Among such devices, GaAs-based Hall sensors, including CYSJ362A [7], are attractive due to their inherently good linearity and robustness compared to Si- or InSb-based sensors. However, their use in liquid nitrogen and at magnetic fields exceeding the specified operating range requires careful experimental validation. Calibration procedures for these sensors under combined cryogenic and high-field conditions are not yet sufficiently standardized, which motivates the systematic investigation presented in this work.

This paper addresses these challenges by presenting a reproducible and uncertainty-aware calibration methodology for CYSJ362A GaAs Hall sensors operating at 77 K and magnetic flux densities above 2 T. The main contributions of this work are:

- a practical coil-based calibration method compatible with cryogenic immersion,
- polynomial regression of the Hall voltage–flux density characteristic,
- comprehensive uncertainty analysis using both analytical error propagation and Monte Carlo simulations.

2. Hall sensor calibration setup

A set of seven CYSJ362A GaAs Hall sensors [7], previously employed in superconductivity-related experiments [8], was selected for calibration. In pulsed-field magnetization experiments, magnetic flux densities exceeding 2 T are generated by currents with steep rise times and long decay times, making individual calibration of each sensor necessary to establish an accurate voltage–field relationship $B(U)$.

The calibration was performed using a non-magnetic solenoid coil with an inductance of $L = 3$ mH. This coil was chosen because it produces the highest peak magnetic field when driven by the flux pump. The calibration procedure consisted of two consecutive steps, i.e., (i) determining the magnetic flux density as a function of current, $B(I)$, at the center of the solenoid, and (ii) mapping the output voltage of each Hall sensor as a function of magnetic flux density. The combination of these relations yields the desired calibration function $B(U)$ for each sensor.

The experimental setup is shown in Fig. 1. A custom 3D-printed holder made of polylactic acid (PLA) was used to position the Hall sensors precisely along the solenoid axis and at the geometric center of the coil, where the axial magnetic field component is most homogeneous. The holder includes a central axial channel that allows insertion of a calibrated reference probe (F71 teslameter, Lake Shore Cryotronics [9]), as well as radial openings to facilitate liquid nitrogen circulation

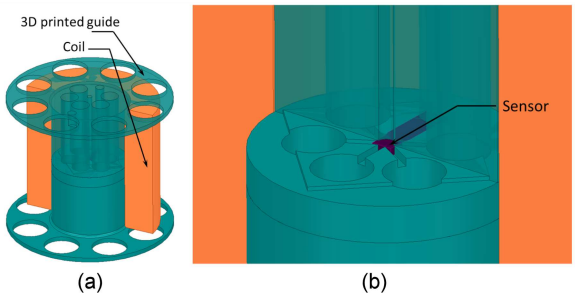

Fig. 1. Calibration setup: (a) coil cross-section with 3D-printed guide; (b) detail of sensor positioning.

and accommodate sensor wiring. The Hall sensors were secured with Kapton tape and mechanically clamped to prevent motion during current pulses.

The current–field calibration of the solenoid, $B(I)$, was carried out at room temperature. In this regime, the magnetic field produced by the air-core solenoid is linear with the current, allowing the measured $B(I)$ relation to be reliably extrapolated beyond the maximum current that could be applied continuously during room-temperature measurements. In the present setup, currents up to approximately 10 A can be applied briefly for calibration. This independently determined $B(I)$ relation serves as a reference for subsequent sensor calibration measurements performed under cryogenic conditions, where higher currents and magnetic fields are reached.

3. Calibration methodology

3.1. Coil characterization

The current versus magnetic flux density characteristic of the calibration solenoid was determined independently of the Hall sensors. All measurements in this step were performed at room temperature using a calibrated reference probe. The Hall sensors played no role during the coil characterization.

Direct-current (DC) tests were conducted by applying currents up to 10 A using a laboratory DC power supply. The current was measured with a calibrated Sanwa PC7000 multimeter [10], while the magnetic flux density at the solenoid center was recorded using an F71 Teslameter (Lake Shore Cryotronics) [9]. For each current level, the magnetic field signal was averaged over a 10 s interval to reduce noise and temporal fluctuations.

The reference probe was inserted into the axial guide of the calibration fixture such that its sensing element coincided with the position later occupied by the calibrated Hall sensor. In this way, the measured $B_L(I)$ relation corresponds directly to the magnetic field experienced by the Hall sensor during subsequent calibration measurements.

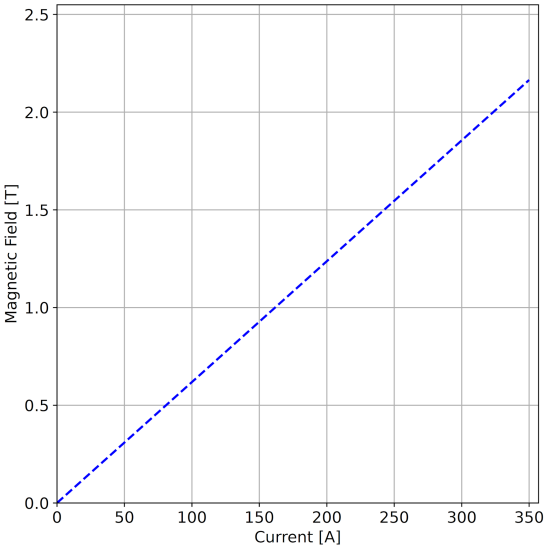

Fig. 2. Extrapolated current–magnetic flux density characteristics.

Measurement uncertainties $u(I)$ and $u(B)$ were determined for each data point based on instrument specifications and statistical variation.

Figure 2 shows the measured current–flux density characteristics and their linear extrapolation. Linear regression was applied to the data, and uncertainties of the fitted parameters were evaluated following the procedure described in [11]. For the solenoid L used in the Hall sensor calibration, the resulting relation is

$$B_L(I) = 6.185(23) \times 10^{-3}\, I - 0.010(14) \times 10^{-3}, \tag{1}$$

where B_L is expressed in tesla [T] and I in amperes [A].

Since the solenoid contains no ferromagnetic materials, the magnetic flux density is proportional to the current over the entire operating range. This linearity allows the $B(I)$ relation obtained at room temperature to be reliably extrapolated beyond the maximum current applied during the DC measurements. The resulting function serves as a reference for converting current waveforms into magnetic flux density during pulsed-field calibration of the Hall sensors.

3.2. Hall sensor calibration under pulsed excitation

In the next step, the relation between the magnetic flux density acting on the Hall sensors and the output voltage was determined under pulsed excitation. This calibration approach was chosen to closely replicate the operating conditions encountered in pulsed-field magnetization experiments, where magnetic flux densities above 2 T are generated by rapidly varying currents.

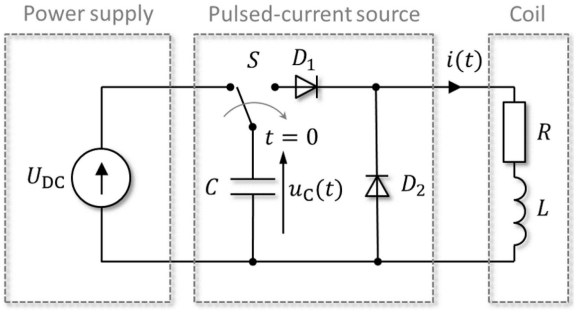

Fig. 3. RLC flux pump used for pulsed-field magnetization.

Each Hall sensor was connected using $\phi 100$ μm twisted copper wires to minimize loop area, mutual inductance, and susceptibility to electromagnetic interference. The sensors operate as voltage dividers and are powered by a regulated laboratory power supply (Aim-TTi QPX600DP) [12] at 10 V. Additional decoupling capacitances of 4.7 μF and 100 nF were connected in parallel at the supply terminals to suppress voltage fluctuations during pulsed operation.

The Hall voltage outputs were recorded using seven passive oscilloscope probes (RIGOL PVP2150) [13], with one probe connected to each sensor. The current waveform driving the calibration coil was measured using a Tektronix TCP404XL current probe connected via a TCPA400 amplifier to a Tektronix MSO3014 mixed-signal oscilloscope [14, 15]. All voltage and current signals were acquired simultaneously, ensuring temporal alignment of the recorded waveforms.

During calibration, the sensors were positioned at the geometric center of the 3D-printed guide (Fig. 1), where the magnetic field is predominantly axial and exhibits the highest degree of homogeneity. The complete assembly, including the solenoid coil, sensors, and holder, was submerged in liquid nitrogen. Magnetic field pulses were generated using the same flux pump system (Fig. 3) employed in pulsed-field magnetization experiments, with a capacitance of $C = 5$ mF and the calibration coil $L = 3$ mH. The coil consisted of $N_{\text{turns}} = 421$, wire diameter was $\phi 1.45$ mm, coil inner diameter $D_{\text{in}} = 35$ mm, outer diameter $D_{\text{out}} = 48.5$ mm, and height $H = 60$ mm. The series resistance of the coil is $R = 0.967\ \Omega$ at a liquid nitrogen temperature of 77 K. This configuration enabled the generation of magnetic flux densities exceeding 2 T, representative of actual operating conditions.

For each sensor, fifteen consecutive magnetic field pulses were applied. Figure 4a and b shows the time-averaged current waveform and the corresponding averaged Hall voltage for a representative sensor (B1), respectively. The averaging was performed at each discrete time point recorded by the

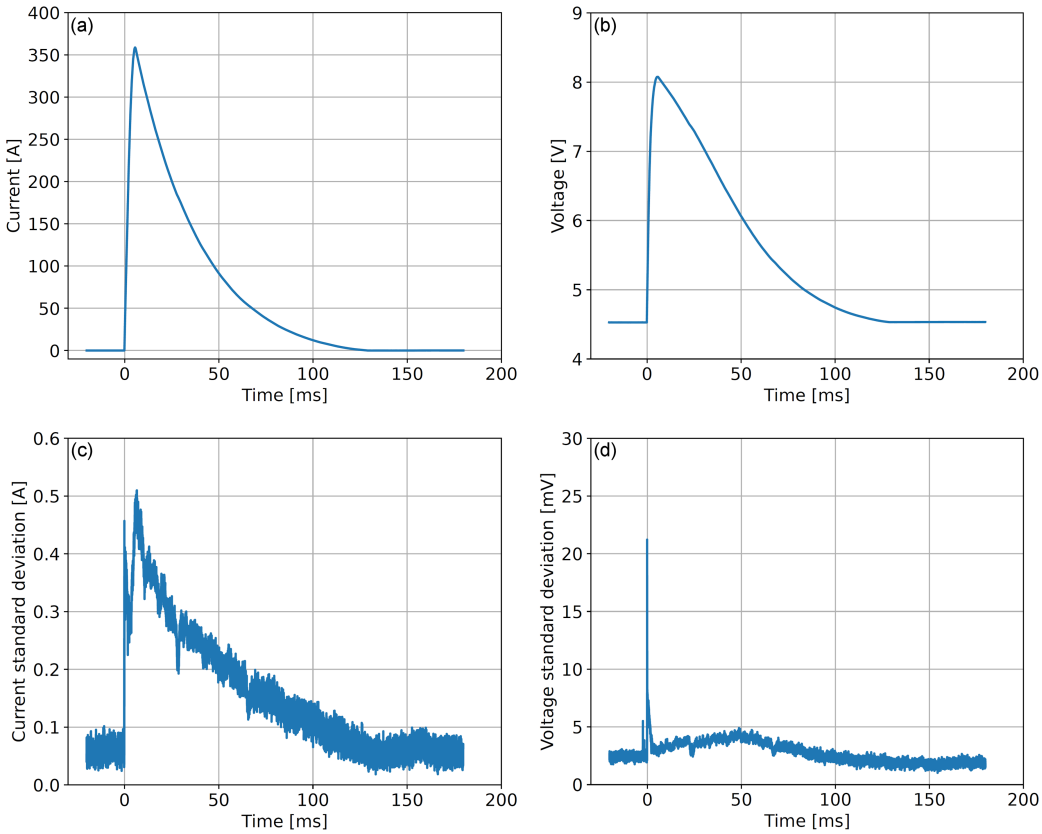

Fig. 4. Statistical analysis of current and voltage waveforms: (a) average current; (b) average voltage (sensor B1); (c) standard deviation of the current waveform; (d) standard deviation of the voltage from the Hall sensor B1.

oscilloscope. From the ensemble of fifteen pulses, the standard deviation of the current and voltage waveforms was calculated at each time step, as shown in Fig. 4c and d. These standard deviations provide an estimate of the Type-A uncertainty associated with the pulsed measurements.

An increased standard deviation is observed at $t = 0$ s, which is attributed to oscilloscope triggering jitter between successive pulses. Later, the standard deviation is significantly reduced, indicating good repeatability of both the applied current pulses and the corresponding Hall voltage measurements.

Since all signals are acquired simultaneously, the measured current and Hall voltage waveforms correspond to the same discrete-time samples. From the averaged waveforms shown in Fig. 4a and b, the voltage–current characteristic of each Hall sensor was obtained (Fig. 5a). Using the previously determined current–flux density relation of the calibration coil (see (1)), the corresponding magnetic flux density acting on the sensor was evaluated for each time sample, yielding the voltage–flux density characteristic shown in Fig. 5b. The resulting characteristics exhibit clear nonlinear behavior.

To enable conversion of the measured Hall voltage to magnetic flux density in subsequent experiments, the inverse relation $B(U)$ was obtained by fitting a polynomial model to the calibration data. Owing to the observed nonlinearity, polynomials of second to seventh order were examined. Model selection was performed using the mean squared error (MSE), coefficient of determination (R^2), Akaike information criterion (AIC), and Bayesian information criterion (BIC). Based on these metrics, a fifth-order polynomial was selected as the optimal compromise between fit quality and model complexity for all sensors.

The resulting calibration function is expressed as

$$B(U) = \sum_{i=0}^{P} b_i \, U^i, \tag{2}$$

where P denotes the polynomial degree.

To determine the polynomial coefficients of the calibration function $B(U)$, the fitting problem was formulated in matrix form using a Vandermonde matrix. For a set of N measured voltage samples U_i and the corresponding magnetic flux density values B_i, the polynomial model of degree P can be written as

$$A\,\boldsymbol{x} = \boldsymbol{b}, \tag{3}$$

where $\boldsymbol{x} = [\,b_0,\, b_1,\, \ldots,\, b_P\,]^{\mathrm{T}}$ is the vector of polynomial coefficients and $\boldsymbol{b} = [\,B_1,\, B_2,\, \ldots,\, B_N\,]^{\mathrm{T}}$ contains the magnetic flux density values obtained from

the coil calibration. The design matrix A is the Vandermonde matrix, defined as

$$A = \begin{bmatrix} 1 & U_1 & U_1^2 & \cdots & U_1^P \\ 1 & U_2 & U_2^2 & \cdots & U_2^P \\ \vdots & \vdots & \vdots & \ddots & \vdots \\ 1 & U_N & U_N^2 & \cdots & U_N^P \end{bmatrix}. \tag{4}$$

Since the system is overdetermined ($N \gg P$), the coefficient vector $\boldsymbol{x}$ was obtained by solving the least-squares problem

$$\boldsymbol{x} = \arg\min_{\boldsymbol{x}} \| \boldsymbol{b} - A\boldsymbol{x} \|_2^2 = A^{\dagger}\boldsymbol{b}, \tag{5}$$

where $A^{\dagger}$ denotes the Moore–Penrose pseudoinverse of the Vandermonde matrix. This approach yields a stable estimate of the polynomial coefficients and allows a straightforward evaluation of the covariance matrix of the fitted parameters, which is later used for uncertainty analysis.

3.3. Polynomial degree selection

Polynomial models of different degrees are evaluated to determine an appropriate trade-off between calibration accuracy and model complexity. Figure 6 shows the dependence of selected goodness-of-fit metrics on polynomial degree for a representative Hall sensor (B1). The remaining sensors exhibited qualitatively identical trends.

The mean squared error (Fig. 6a) decreases rapidly with increasing polynomial degree and exhibits only marginal improvement beyond fourth order, with a shallow minimum observed at the fifth-order model. The coefficient of determination (Fig. 6b) increases monotonically, approaching saturation as expected for nested polynomial models, and provides limited discrimination between higher-order fits.

In contrast, the Akaike (Fig. 6c) and Bayesian (Fig. 6d) information criteria, which explicitly penalize model complexity, reach a clear minimum at the fifth-order polynomial. This indicates that higher-order models do not provide a statistically significant improvement relative to their increased complexity. Based on these considerations, a fifth-order polynomial was selected as the optimal compromise between calibration accuracy and model simplicity for all sensors.

3.4. Uncertainty analysis

3.4.1. Uncertainty of the polynomial fit

The uncertainty associated with the polynomial calibration function arises from the finite number of measurements used in the regression and is quantified using least-squares estimation theory. For every applied pulse, the current waveform $i(t)$ and the corresponding Hall voltage waveform $u(t)$ were recorded simultaneously. Using the previously determined coil calibration function $B(I)$, the current waveforms were converted into magnetic flux density waveforms $B(t)$. At each discrete time sample, the mean values $\overline{B}(t)$ and $\overline{U}(t)$, as well as their standard deviations, were calculated from the ensemble of pulses.

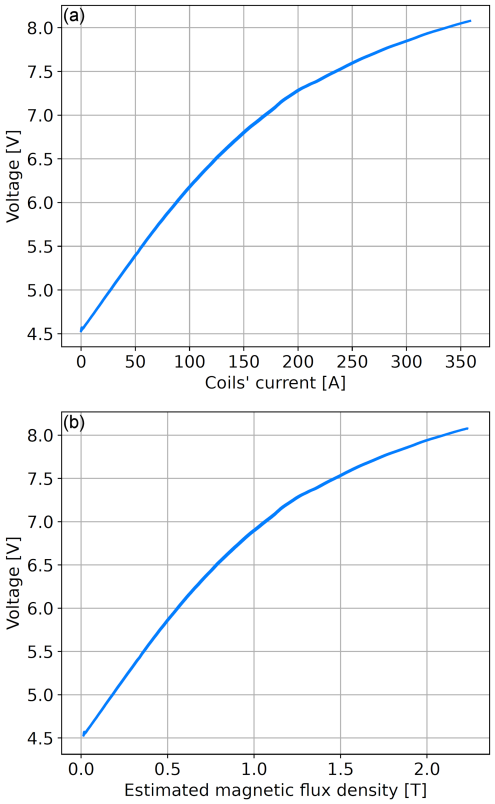

Fig. 5. (a) Dependence between voltage reading from Hall sensor B1 and current applied to the coil; (b) dependence between voltage reading from Hall sensor B1 and estimated magnetic flux density acting on sensor B1.

The averaged voltage–flux density data pairs $\{U_i, B_i\}$ were used to determine the calibration function $B(U)$ by polynomial regression. Due to the finite number of measurements and pulse-to-pulse variations, the fitted polynomial coefficients are subject to statistical uncertainty. This uncertainty was quantified using standard least-squares estimation theory.

Let the polynomial model be written in matrix form as

$$A\,\boldsymbol{x} = \boldsymbol{b}, \tag{6}$$

where A is the Vandermonde matrix constructed from the measured voltage samples U_i, $\boldsymbol{x}$ is the vector of polynomial coefficients, and $\boldsymbol{b}$ contains the corresponding magnetic flux density values. The residual vector is defined as

$$\boldsymbol{r} = \boldsymbol{b} - A\,\boldsymbol{x}. \tag{7}$$

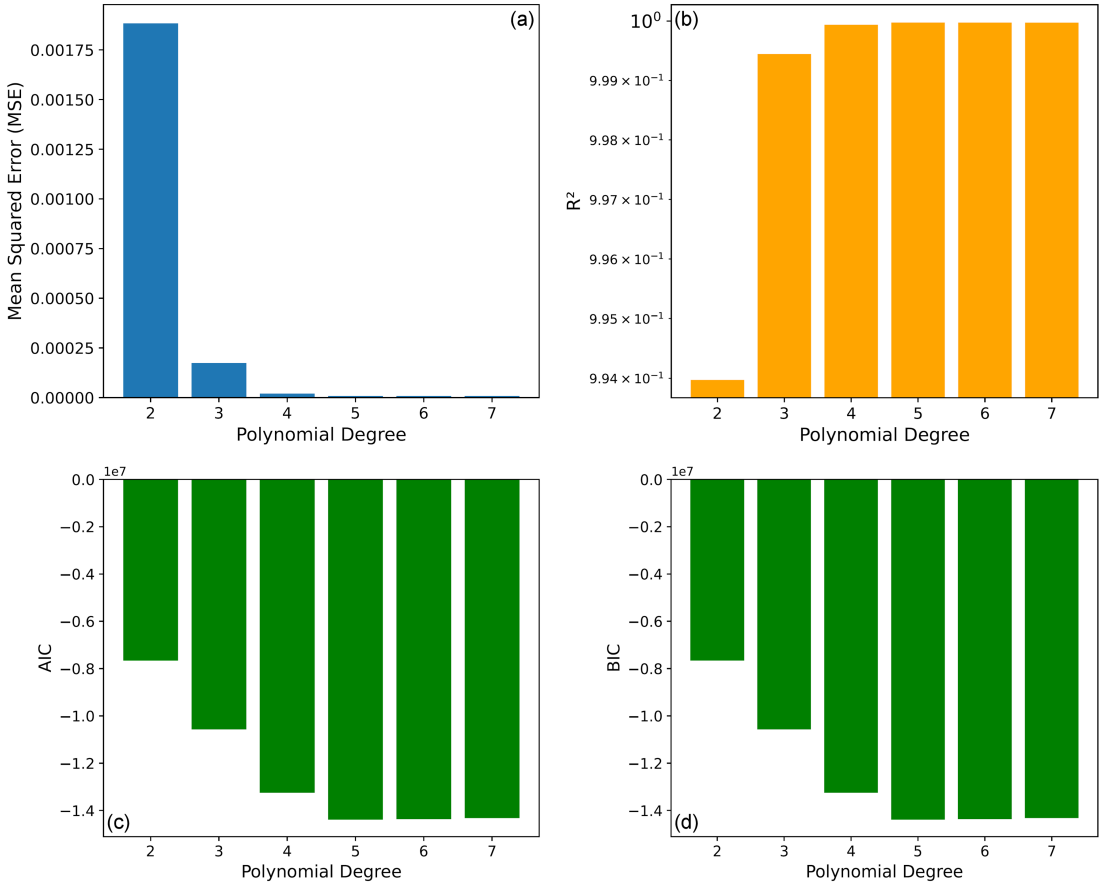

Fig. 6. Goodness-of-fit metrics used for polynomial degree selection for a representative Hall sensor (B1): (a) mean squared error (MSE); (b) coefficient of determination (R^2); (c) Akaike information criterion (AIC); (d) Bayesian information criterion (BIC).

TABLE I

Polynomial coefficients b_i of the calibration function of a fifth-order polynomial for individual Hall sensors.

Sensor	b_0 [T]	b_1 [T/V]	b_2 [T/V^2]	b_3 [T/V^3]	b_4 [T/V^4]	b_5 [T/V^5]
1	−30.495(32)	26.221(27)	−9.2336(90)	1.6467(15)	−0.14715(12)	0.0052902(39)
2	−31.366(29)	27.001(24)	−9.5117(79)	1.6962(13)	−0.15152(11)	0.0054447(34)
3	−29.452(47)	25.358(39)	−8.9548(13)	1.6026(22)	−0.14373(18)	0.0051870(57)
4	−32.470(33)	28.044(28)	−9.8965(95)	1.7667(16)	−0.15797(13)	0.0056817(42)
5	−31.008(28)	26.746(24)	−9.4435(79)	1.6883(13)	−0.15121(11)	0.0054488(35)
6	−30.507(29)	26.285(24)	−9.2745(81)	1.6573(13)	−0.14838(11)	0.0053453(35)
7	−30.729(44)	26.495(37)	−9.3564(12)	1.6735(20)	−0.14998(17)	0.0054089(54)

Assuming independent and identically distributed measurement errors, the variance of the residuals was estimated as

$$\sigma^2 = \frac{\boldsymbol{r}^{\mathrm{T}}\boldsymbol{r}}{N-P}, \tag{8}$$

where N is the number of data points, and P is the degree of the polynomial. The covariance matrix of the fitted polynomial coefficients is then given by

$$\mathrm{cov}(\boldsymbol{x}) = \sigma^2\left(A^{\mathrm{T}}A\right)^{-1}. \tag{9}$$

Although the residual variance σ^2 is estimated from statistical scatter of the data, the resulting covariance of the polynomial coefficients represents a model-based uncertainty contribution and is therefore treated as Type-B uncertainty. The standard uncertainties of the individual polynomial coefficients are obtained as the square roots of the diagonal elements of the covariance matrix,

$$u(\boldsymbol{x}) = \sqrt{\mathrm{diag}\left(\mathrm{cov}(\boldsymbol{x})\right)}. \tag{10}$$

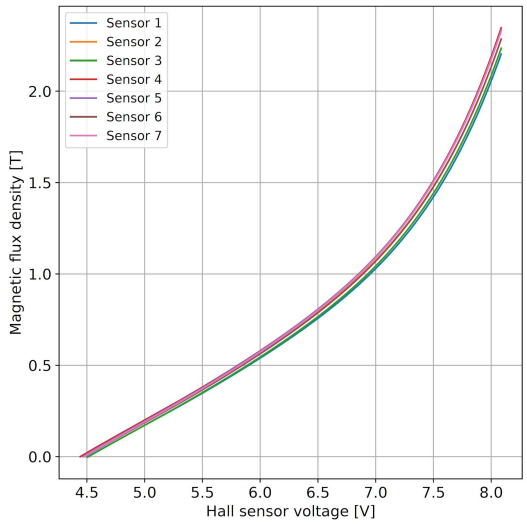

Fig. 7. Polynomial fits for all calibrated sensors with supply voltage 10 V in liquid nitrogen (77 K).

To propagate the coefficient uncertainties into the uncertainty of the estimated magnetic flux density, the law of propagation of uncertainty was applied. For a given voltage value, U, the sensitivity vector

$$\boldsymbol{g}(U) = \begin{bmatrix} 1 & U & U^2 & \cdots & U^P \end{bmatrix}^{\mathrm{T}} \tag{11}$$

was defined. The resulting uncertainty contribution of the polynomial fit to the magnetic flux density estimate is then

$$u_{\mathrm{B}}^2\left(B(U)\right) = \boldsymbol{g}^{\mathrm{T}}(U)\,\mathrm{cov}(\boldsymbol{x})\,\boldsymbol{g}(U). \tag{12}$$

This contribution reflects the statistical uncertainty associated with the finite number of pulsed measurements and the polynomial regression procedure.

The fitted coefficients for all seven sensors, including uncertainties, are listed in Table I, and the plotted polynomials are shown in Fig. 7.

3.4.2. Uncertainty of magnetic flux density estimation

To estimate the uncertainty associated with the magnetic field generated by the calibration coil, a numerical model based on the Biot–Savart law was used. The calibration coil was represented as a set of circular current loops corresponding to individual turns. Each turn was discretized into a finite number of straight current segments, allowing for a numerical evaluation of the magnetic field at the sensor location.

The magnetic flux density contribution $\mathrm{d}B$ from a current element $\mathrm{d}\boldsymbol{\ell}$ carrying current I was computed using the Biot–Savart law,

$$\mathrm{d}B = \frac{\mu_0 I}{4\pi}\frac{\mathrm{d}\boldsymbol{\ell}\cdot\hat{\boldsymbol{r}}}{|\boldsymbol{r}|^2}, \tag{13}$$

where $\boldsymbol{r}$ denotes the vector from the current element to the observation point and $\hat{\boldsymbol{r}} = \boldsymbol{r}/|\boldsymbol{r}|$.

A cylindrical coordinate system (r, θ, z) was adopted, with the z-axis aligned with the axis of the solenoid. The magnetic field was evaluated at the position of the Hall sensor, which was located on the solenoid axis and at the geometric center of the coil along its length. The total magnetic flux density was obtained by summing the contributions of all current elements over the entire coil.

The same Biot–Savart-based numerical model was used to quantify the associated Type-B uncertainty. The calibration coil was represented as a set of circular current loops corresponding to individual turns. Each turn was discretized into a finite number of straight current segments, enabling numerical evaluation of the magnetic field at the sensor location.

In the discrete formulation, the magnetic flux density contribution ΔB from a current segment $\Delta\boldsymbol{\ell}$ carrying current I is given by

$$\Delta B = \frac{\mu_0 I}{4\pi}\frac{\Delta\boldsymbol{\ell}\cdot\hat{\boldsymbol{r}}}{|\boldsymbol{r}|^2}, \tag{14}$$

where $\boldsymbol{r}$ denotes the vector from the center of the current segment to the observation point, and $\hat{\boldsymbol{r}} = \boldsymbol{r}/|\boldsymbol{r}|$. This expression represents the discrete counterpart of the continuous Biot–Savart law and is well suited for numerical summation.

A cylindrical coordinate system (r, θ, z) was adopted, with the z-axis aligned with the solenoid axis. Each coil turn was modeled as a circle of radius r_{turn} and discretized uniformly in the angular coordinate θ. The Hall sensor was located at position $(r_{\mathrm{sens}}, 0, 0)$, corresponding to the axial center of the coil, where the magnetic field is predominantly oriented along the z-direction.

The total magnetic flux density at the sensor position was obtained by summing the contributions of all current segments over all turns of the coil,

$$B = \sum_{k=1}^{N_{\mathrm{turn}}}\sum_{j=1}^{N_\theta}\Delta B_{k,j}, \tag{15}$$

where N_{turn} is the number of coil turns, and N_θ is the number of angular subdivisions per turn.

In the numerical model, the magnetic flux density generated by the calibration coil for a given current I was evaluated by summing the contributions of all discretized current segments over all turns of the coil,

$$B(I) = \sum_{i=1}^{N_{\mathrm{turn}}}\sum_{j=1}^{N_\theta}\Delta B_{ij} = \sum_{i=1}^{N_{\mathrm{turn}}}\sum_{j=1}^{N_\theta}\frac{\mu_0 I}{4\pi}\frac{\Delta\boldsymbol{\ell}_{ij}\cdot\hat{\boldsymbol{r}}_{ij}}{|\boldsymbol{r}_{ij}|^2}, \tag{16}$$

where $N_{\mathrm{turn}} = 421$ denotes the number of turns and N_θ the number of angular subdivisions per turn. The vectors $\Delta\ell_{ij}$ and r_{ij} correspond to the j-th current segment of the i-th turn and the vector from this segment to the sensor position, respectively. A pictorial representation of the approach is shown in Fig. 8.

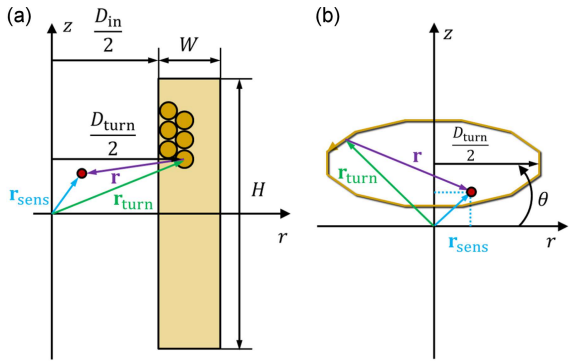

Fig. 8. (a) Biot–Savart law applied to the i-th turn; (b) Biot–Savart law applied to the j-th segment of the i-th turn.

In addition to geometric uncertainties, the uncertainty of the current flowing through the coil contributes to the Type-B uncertainty of the generated magnetic field. The Tektronix TCP404XL current probe with a TCPA400 amplifier was used to measure and capture current waveforms. Based on the ensemble of pulsed measurements described in the previous section, the statistical variability of the measured current was used to estimate its standard deviation.

The Monte Carlo simulation combines statistical contributions from repeated pulsed measurements (Type-A) with model-based contributions from current measurement, coil geometry, and sensor positioning (Type-B). The resulting uncertainty is therefore treated as a combined standard uncertainty.

For the Monte Carlo simulation, the current I was treated as a normally distributed random variable,

$$I \sim \mathcal{N}\left(\overline{I},\, u^2(I)\right), \tag{17}$$

where $\overline{I}$ is the mean current value and $u(I)$ denotes its standard uncertainty. The relative standard uncertainty of the current was estimated to be $\approx 3\%$, based on the datasheet of the TCPA400 system [14]. The dot notation in $\mathcal{N}(\,\cdot\,;\,3\%)$ indicates that this distribution applies to any instantaneous current value flowing through the coil.

For each Monte Carlo realization, a current value was sampled from (17) and used in (16) to compute the corresponding magnetic flux density at the sensor position.

The contribution of current measurement uncertainty to the Type-B uncertainty of the magnetic flux density was analyzed using the previously described ensemble of pulsed measurements. Figure 9a shows the Type-A uncertainty of the measured current, obtained as the standard deviation of the current waveforms from fifteen repeated pulses. This contribution is most pronounced at lower current values, where triggering jitter and pulse-to-pulse variability have a larger relative impact.

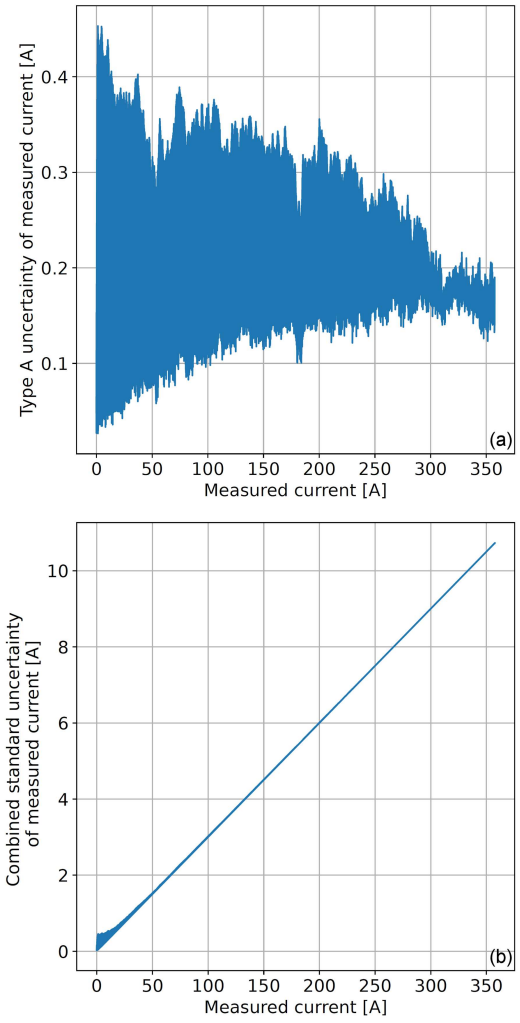

Fig. 9. Current measurement uncertainty: (a) Type-A uncertainty estimated from repeated pulsed measurements; (b) combined standard uncertainty of the measured current as a function of current amplitude.

Figure 9b, in turn, illustrates the combined standard uncertainty of the measured current as a function of current amplitude. At higher current levels, the uncertainty is dominated by the Type-B contribution associated with the current measurement system. In particular, the relative standard uncertainty of approximately 3%, estimated from the characteristics of the Tektronix TCP404XL probe and TCPA400 amplifier, becomes the dominant component of the total uncertainty budget.

As a result, the uncertainty of the current measurement exhibits an approximately linear dependence on the current magnitude in the high-field regime. This behavior directly propagates into the magnetic flux density uncertainty through the Biot–Savart model used in the Monte Carlo simulation. At lower current values, the Type-A contribution remains non-negligible, whereas at high currents relevant for pulsed-field magnetization experiments,

the Type-B contribution, corresponding to a relative uncertainty of approximately 3%, dominates at high current values.

In addition to current uncertainty, geometric imperfections of the calibration coil contribute to the Type-B uncertainty of the magnetic flux density. Since the calibration coil is a real, manufactured object, deviations from its idealized geometry must be accounted for. To quantify these effects, the coil was measured directly using precision calipers.

The inner diameter D_{in}, coil thickness $W = D_{\mathrm{out}}/2 - D_{\mathrm{in}}/2$, and coil height H were measured at multiple positions along the circumference and axial direction of the coil. The results revealed that the dominant contributor to the uncertainty in the diameters arises from shape irregularities and the non-circularity of the winding rather than from measurement repeatability. Consequently, the Type-A uncertainty dominates for the diameter-related quantities. In contrast, the coil height H showed significantly greater uniformity, resulting in a smaller associated uncertainty.

The combined standard uncertainty of the effective turn diameter D_{turn} was determined from the independently measured inner diameter and coil thickness according to

$$u_c(D_{\mathrm{turn}}) = \sqrt{u_c^2(D_{\mathrm{in}}) + u_c^2(W)}. \tag{18}$$

Based on the experimental measurements, this yielded a combined standard uncertainty of approximately 0.6×10^{-3} m for the turn diameter.

The coil was wound using copper wire with a nominal diameter of 1.45 mm. In the numerical model, each turn was therefore treated as occupying a finite radial and axial extent rather than an infinitesimally thin loop. To account for this, the radial position of each turn was modeled as a random variable drawn from a normal distribution centered at the nominal turn radius,

$$r_{\mathrm{turn}} \sim \mathcal{N}\left(\overline{r}_{\mathrm{turn}},\, u_c^2(r_{\mathrm{turn}})\right), \tag{19}$$

where $u_c(r_{\mathrm{turn}})$ is derived from the measured uncertainty of D_{turn}.

Similarly, the axial position of each turn was modeled as a normally distributed random variable to reflect uncertainties in turn stacking and wire placement along the z-axis,

$$z_{\mathrm{turn}} \sim \mathcal{N}\left(\overline{z}_{\mathrm{turn}},\, u_c^2(z_{\mathrm{turn}})\right), \tag{20}$$

with the standard uncertainty determined from the measured coil height H and the number of turns.

In the Monte Carlo simulation, the geometric parameters for each turn were sampled independently of the distributions above. For each realization, a unique coil geometry was generated by assigning individual radial and axial positions to all turns, after which the magnetic flux density was computed using the discrete Biot–Savart formulation described previously. This approach enables propagation of geometric uncertainties into the magnetic field estimate in a physically consistent manner.

In addition to uncertainties in current and coil geometry, the Hall sensor position relative to the calibration coil was included in the Monte Carlo simulation. Although the sensor was nominally positioned at the geometric center of the coil and aligned with the solenoid axis, small misalignments arising from manufacturing tolerances of the holder, wire routing, and assembly cannot be ruled out.

The nominal sensor position was defined as $(r, z, \theta) = (0, 0, 0)$ in the cylindrical coordinate system. Deviations from this ideal position were modeled as independent normally distributed random variables in the radial, axial, and angular directions. The corresponding distributions were defined as

$$\begin{aligned} r_{\mathrm{sens}} &\sim \mathcal{N}\left(0,\, u_c^2(r_{\mathrm{sens}})\right), \\ z_{\mathrm{sens}} &\sim \mathcal{N}\left(0,\, u_c^2(z_{\mathrm{sens}})\right), \\ \theta_{\mathrm{sens}} &\sim \mathcal{N}\left(0,\, u_c^2(\theta_{\mathrm{sens}})\right), \end{aligned} \tag{21}$$

where the standard uncertainties were derived from mechanical tolerances of the sensor holder and positioning procedure.

A conservative confidence level of 99% was assumed for the sensor position uncertainty, corresponding to a coverage factor of $k_\alpha = 2.576$. The resulting standard uncertainties were $u_c(r_{\mathrm{sens}}) = 0.39 \times 10^{-3}$ m for radial displacement, $u_c(z_{\mathrm{sens}}) = 0.28 \times 10^{-3}$ m for axial displacement, and $u_c(\theta_{\mathrm{sens}}) = 5^\circ$ for angular misalignment. This represents a worst-case assumption intended to avoid underestimation of the Type-B uncertainty.

Together with the previously defined random variables for coil current, turn radius, and axial wire position, these distributions define the complete input parameter set of the Monte Carlo simulation. For each realization, independent samples were drawn for all parameters, generating a unique coil–sensor configuration. The magnetic flux density was then computed using the discrete Biot–Savart formulation, yielding an ensemble of magnetic field values from which the Type-B uncertainty contribution was determined.

An example result of the Monte Carlo simulation is shown in Fig. 10 for an applied current of $I = 100$ A. In this case, 10^6 independent Monte Carlo realizations were performed. In each realization, a complete set of input parameters was sampled from the distributions defined in the previous sections, including coil current, wire positions, coil geometry, and sensor position. The magnetic flux density at the sensor location was then computed using the discrete Biot–Savart model.

The resulting distribution of magnetic flux density values is approximately normal. From this distribution, the mean magnetic flux density and its standard uncertainty were extracted as the sample mean and standard deviation, respectively. For $I = 100$ A, the simulation yields

$$B_{\mathrm{MC}}(I = 100\ \mathrm{A}) = 617.5(65) \times 10^{-3}\ \mathrm{T}. \tag{22}$$

For reference, the mean value obtained from the Monte Carlo simulation is consistent with the magnetic flux density predicted by linear extrapolation of the experimentally determined coil calibration function previously obtained using the F71 reference probe at room temperature (see (1)). The Monte Carlo result thus validates the extrapolated $B(I)$ relation while providing a statistically robust estimate of the associated Type-B uncertainty.

This example demonstrates how the combined effects of current uncertainty, geometric tolerances, and sensor positioning uncertainty contribute to the overall uncertainty in the magnetic flux density. The same procedure was applied for the full range of currents used in the Hall sensor calibration.

4. Results

The Monte Carlo simulation of the calibration coil was performed for a discrete set of current values representative of the operating range used during Hall sensor calibration. Simulations were carried out for nominal current values $\hat{I} = 50$–350 A in steps of 50 A, with an additional point at $\hat{I} = 10$ A to capture the lower end of the current range. For each selected current value, 10^6 Monte Carlo realizations were generated by sampling all input parameters according to the distributions defined in the previous section.

The current measurement uncertainty was modeled using a normal distribution with a relative standard uncertainty of approximately 3%, consistent with the characteristics of the TCP404XL/TCPA400 current measurement system [14]. For each Monte Carlo realization, a unique set of current, coil geometry, and sensor position parameters was generated, and the corresponding magnetic flux density at the sensor location was computed using the discrete Biot–Savart model.

An example of the resulting magnetic flux density distribution for $\hat{I} = 100$ A is shown in Fig. 10. The distribution is approximately normal. The standard uncertainty of the magnetic flux density associated with the Monte Carlo simulation, $u_{c2}(B(I))$, was evaluated as the standard deviation of the simulated magnetic flux density values for each current level.

The combined standard uncertainty of the magnetic flux density, $u_c(B)$, was obtained by combining the uncertainty associated with the Hall voltage measurement (Fig. 4d) and polynomial calibration (12). The combined uncertainty from voltage and polynomial fit $u_{c1}(B(U))$ is given by

$$u_{c1}^2\left(B(U)\right) = \underbrace{\left(\frac{\mathrm{d}B}{\mathrm{d}U}\right)^2 u^2(U)}_{\substack{\text{Type-A uncertainty}\\ \text{Statistical uncertainty}\\ \text{(Hall voltage measurement)}}} + \underbrace{\boldsymbol{g}^{\mathrm{T}}(U)\,\mathrm{cov}(\boldsymbol{x})\,\boldsymbol{g}(U)}_{\substack{\text{Type-B uncertainty}\\ \text{(polynomial fit coefficient covariance)}}} . \tag{25}$$

To avoid double-counting of uncertainty contributions, pulse-to-pulse current variability is incorporated exclusively through the Monte Carlo simulation and is not added separately to the uncertainty budget. The resulting Monte Carlo standard deviation accounts for both statistical variability of the measured current and model-based contributions from coil geometry and sensor positioning; it is therefore treated as a combined standard uncertainty. Accordingly, $u_{c2}(B(I))$ is evaluated using

$$u_{c2}^2\left(B(I)\right) = \mathrm{std}^2\left(B_{\mathrm{MC}}(I)\right). \tag{26}$$

The total combined uncertainty of the measured magnetic flux density B for a calibrated sensor is given by

$$u_c(B) = \sqrt{u_{c1}^2\left(B(U)\right) + u_{c2}^2\left(B(I)\right)}. \tag{27}$$

For each simulated current value, the corresponding mean voltage reading was obtained from the measured current and voltage waveforms (Fig. 4), and the combined standard uncertainty of the voltage, $u_c(U)$, was evaluated. The resulting magnetic flux density–voltage characteristics, including combined uncertainty bounds, are shown in Fig. 11. The Monte Carlo simulation was performed for discrete current values $\hat{I} = 50$–350 A in steps of 50 A, with an additional simulation at $\hat{I} = 10$ A to capture the low-current regime. For each nominal current value $\hat{I}$, 10^6 Monte Carlo realizations were generated. Error bars indicate the combined standard uncertainty of the magnetic flux density at each operating point.

5. Discussion

A relevant reference for comparison is the cryogenic calibration study by Chen et al. [6], who investigated the temperature-dependent behavior of a Hall probe over a magnetic field range of ±1.9 T and temperatures from 2.8 to 300 K under steady-state conditions. Their results show that Hall sensor nonlinearity becomes significant above approximately 0.5 T, reaching about 5% at ±1.8 T. This behavior is qualitatively consistent with the nonlinear voltage–flux density characteristics observed in the present work for magnetic flux densities exceeding 2 T.

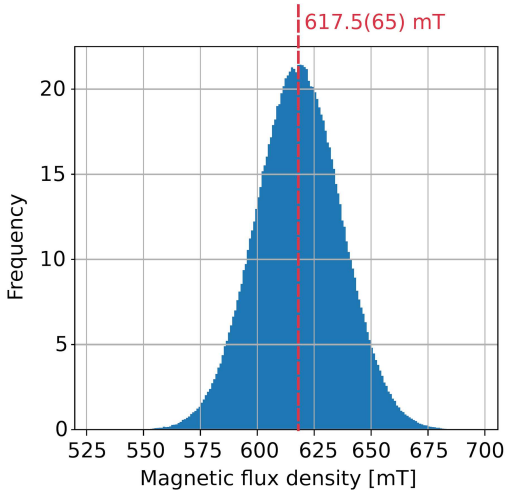

Fig. 10. Histogram of magnetic flux density obtained from 10^6 Monte Carlo realizations for an applied current of $\hat{I} = 100$ A.

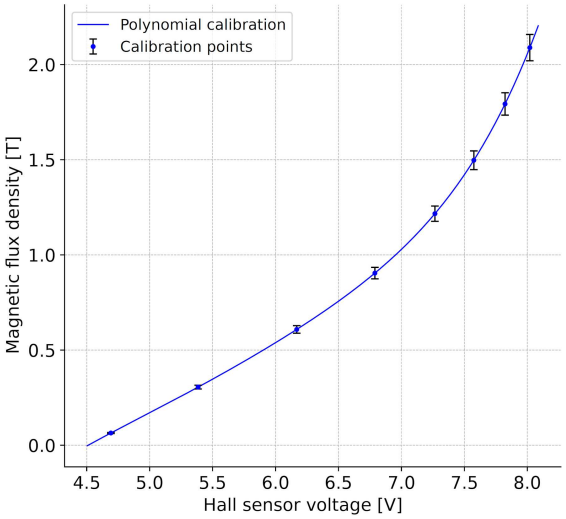

Fig. 11. Magnetic flux density–voltage characteristic of Hall sensor B1 with combined standard uncertainty bars obtained from Monte Carlo simulation and voltage measurement uncertainty.

Chen et al. focused on steady-state magnetic fields and dedicated cryogenic Hall probes, whereas the present work addresses low-cost GaAs Hall sensors operating outside their specified range under pulsed excitation and multi-tesla magnetic fields. Consequently, the higher combined uncertainty reported here reflects additional contributions from transient current measurement, coil geometry, and sensor positioning, and should be interpreted as a conservative upper bound appropriate for pulsed-field magnetization experiments.

Commercial cryogenic Hall probes, such as the Lake Shore HGCA-3020 and HGCT-3020 series, are typically specified to exhibit linearity errors on the order of ±1–2% of full scale over fields up to approximately ±3 T, with sensitivity variations of about 0.7–1% across cryogenic temperatures. These values provide representative performance benchmarks for instrumentation-grade sensors.

In the present work, low-cost GaAs Hall sensors operating at 77 K under pulsed magnetic fields above 2 T exhibit combined standard uncertainties of up to approximately 10% under conservative assumptions of 99% confidence level, which is not typically specified by the manufacturer. The comparison indicates that the dominant uncertainty contributions arise from current measurement and dynamic effects inherent to pulsed operation, rather than from intrinsic Hall sensor nonlinearity alone.

Alternative high-accuracy approaches based on closed-loop zero-flux configurations have also been reported. For example, Liu et al. [16] demonstrated a zero-flux Hall current sensor operating at 77 K with an accuracy class of approximately 1.0 for currents up to 8 kA. While such systems achieve high accuracy, they rely on active compensation, additional magnetic components, and dedicated control electronics, which are incompatible with the open-loop, multi-point sensing requirements of pulsed-field magnetization experiments.

Polynomial calibration has also been shown to reduce Hall sensor nonlinearity under controlled conditions. Klaykabil et al. [17] reported an overall uncertainty of approximately 0.15% for three-axis Hall sensors calibrated in uniform, steady magnetic fields over a limited temperature range. In contrast, the present study addresses calibration at liquid nitrogen temperature under pulsed excitation and in multi-tesla fields, where additional uncertainty contributions are unavoidable and reflect a more demanding experimental environment.

The current measurement during calibration was performed using a TCP404XL current probe and TCPA400 amplifier. Although higher absolute accuracy could in principle be achieved with a precision shunt resistor under steady-state conditions, a current probe was deliberately chosen to match the experiment's dynamic operating regime and to avoid perturbing the pulsed circuit.

The calibration pulses were applied with the coil fully submerged in liquid nitrogen and exhibited peak currents of approximately 350 A with a pulse duration of about 120 ms. The current reached its maximum value within approximately 4 ms, corresponding to a characteristic frequency of the order of 60 Hz. Under these conditions, the coil operates in a strongly transient regime, with an electrical time constant $\tau = L/R \approx 31$ ms for $L = 3$ mH and $R \approx 97$ mΩ at 77 K.

In such a regime, using a shunt resistor is complicated by several factors. First, the parasitic inductance of the shunt element and its connections introduces additional voltage components proportional to $\mathrm{d}I/\mathrm{d}t$, resulting in frequency-dependent

measurement errors. Second, the insertion of a shunt and its terminals adds series resistance and inductance to the discharge circuit, thereby modifying the effective circuit parameters and altering the current pulse shape, rise time, and peak value. This effect is particularly relevant when calibration is intended to reproduce the same electrical conditions encountered during actual pulsed-field operation.

An additional limitation arises from thermal effects. The coil leads, cooled to liquid nitrogen temperature, act as efficient thermal conductors, establishing a strong temperature gradient along the current path. If a shunt resistor were inserted into this path, its temperature would be influenced simultaneously by Joule heating during the pulse and conductive cooling through the cold leads. This would result in time-dependent, spatially non-uniform resistance variations that cannot be reliably corrected by static calibration.

In contrast, the clamp-on current probe used in this work provides galvanic isolation, negligible circuit perturbation, and thermal decoupling from the cryogenic environment, operating under stable room-temperature conditions. The associated relative uncertainty of approximately 3% was propagated through the calibration procedure via Monte Carlo simulation. This ensures that the current measurement uncertainty is fully accounted for in the calibrated magnetic flux density.

6. Conclusions

A calibration methodology for low-cost CYSJ362A GaAs Hall sensors operating under cryogenic and high-field conditions has been presented. The sensors were calibrated at liquid nitrogen temperature (77 K) and magnetic flux densities exceeding 2 T using a coil-based reference setup. The relationship between Hall voltage and magnetic flux density was modeled using a polynomial, enabling direct conversion of measured voltage signals into magnetic field values under pulsed excitation.

Polynomial models of fourth to sixth order were evaluated for the sensor calibration. A quantitative comparison using the mean squared error, coefficient of determination (R^2), Akaike information criterion (AIC), and Bayesian information criterion (BIC) showed that a fifth-degree polynomial provides the best compromise between accuracy and model complexity for the observed nonlinear sensor characteristics.

A comprehensive uncertainty analysis was performed by combining the statistical uncertainty of the polynomial regression with a Monte Carlo simulation of the calibration coil. The Monte Carlo model incorporated uncertainties in coil current measurement, coil geometry, wire placement, and sensor positioning, assuming conservative worst-case conditions. The dominant contributor to the overall uncertainty was the current measurement uncertainty, estimated to be approximately 3% based on the specifications of the TCP404XL/TCPA400 measurement system [14], while geometric tolerances, sensor placement, and regression-related effects contributed smaller but non-negligible components.

For magnetic flux densities above 2 T, the combined standard uncertainty of the calibrated magnetic field was approximately 10%, corresponding to a conservative worst-case scenario assuming a 99% confidence level for sensor positioning and geometric tolerances. Despite this relatively high uncertainty at extreme operating conditions, the calibrated sensors exhibited good repeatability and stable behavior across multiple measurements. The results demonstrate that, when combined with appropriate calibration and uncertainty quantification, low-cost GaAs Hall sensors can be reliably used in pulsed-field magnetization experiments on high-temperature superconductors, particularly in applications requiring multi-point magnetic field measurements.

References

[1] I. Vasil'evskii, A. Vinichenko, M. Strikhanov et al., *IOP Conf. Ser. Mater. Sci. Eng.* **475**, 012015 (2019).

[2] H. Wei, Q. Wang, L. Hao, J. Hu, I. Patel, A. Shah, Y. Wu, Z. Huang, T. Coombs, *IEEE Trans. Appl. Supercond.* **34**, 5203005 (2024).

[3] Z. Huang, H.S. Ruiz, Y. Zhai, J. Geng, B. Shen, T.A. Coombs, *IEEE Trans. Appl. Supercond.* **26**, 1 (2016).

[4] A.A. Caunes, T. Ida, M. Watasaki, M. Izumi, *J. Phys. Conf. Ser.* **1975**, 012018 (2021).

[5] Y. Wang, M.D. Ainslie, D. Zhou, Y. Zhang, C. Cai, J.H. Durrell, D.A. Cardwell, *Supercond. Sci. Technol.* **36**, 075006 (2023).

[6] J. Chen, J. Zhang, Q. Zhou, *Nucl. Instrum. Methods Phys. Res. A* **1062**, 169169 (2024).

[7] CYSJ362A GaAs Hall Effect Element, ChenYang Technologies GmbH & Co. KG, 2016.

[8] J. Gnilsen, A. Usoskin, M. Eisterer, U. Betz, K. Schlenga, *Supercond. Sci. Technol.* **32**, 104002 (2019).

[9] F71 and F41 Teslameters — Technical Specifications, Lake Shore Cryotronics, 2019.

[10] Digital Multimeter PC7000, Sanwa Electric Instrument Co., Ltd..

[11] L. Kirkup, R.B. Frenkel, *An Introduction to Uncertainty in Measurement*, Cambridge University Press, Cambridge 2006.

[12] Bench/System DC Power Supply QPX600DP — Technical Datasheet, Aim TTi.

[13] PVP2150 150 MHz Passive Oscilloscope Probe — Datasheet, Rigol Technologies Co., Ltd..

[14] AC/DC Current Measurement Systems — TCPA300/TCPA400 Series Datasheet, Tektronix, Inc..

[15] Mixed Signal Oscilloscopes — MSO3000/DPO3000 Series Datasheet, Tektronix, Inc..

[16] P. Liu, W. Wang, L. Zhou, M. Zhao, C. Wu, L. He, H, Liu, *IEEE Trans. Appl. Supercond.* **35**, 1 (2025).

[17] W. Klaykabil, T. Yan, H. Bouquet, W. Gil, K. Khosonthongkee, J. Srisertpol, in: *2025 IEEE 17th Int. Conf. on Electronic Measurement & Instruments (ICEMI)*, 2025, p. 211.